X-ray computed tomography and laminography measurements of a 3D-stacked IC

Felix H. Kim[1*], Orion Kafka[2†], Istiaq F. Shiam[3‡], Adam L. Pintar[1], John Henry J. Scott[1], John A. Wu[1, 4], Jessie Zhang[1], and Navid Asadizanjani[3]
[1]National Institute of Standards and Technology, 100 Bureau Dr., Gaithersburg, MD 20899 USA
[2]National Institute of Standards and Technology, 325 Broadway, Boulder, CO 80305 USA
[3]University of Florida, Gainesville, FL 32611 USA
[4]Georgetown University, 3700 O St. NW, Washington, DC 20057 USA
[*]Email: felix.kim@nist.gov
[†]Currently with QuesTek Innovations, LLC.
[‡]Currently with ficonTec

Abstract
Advanced semiconductor packages manufactured using heterogeneous integration techniques challenge many conventional non-destructive testing processes. A three-dimensional (3D) structure of stacked integrated circuits (ICs), for example, complicates many existing non-destructive testing techniques. X-ray-based imaging methods, on the other hand, can fully penetrate the part and are ideal for visualizing the complex 3D heterogeneity. In this research, two related X-ray-based 3D imaging techniques, X-ray computed tomography (XCT) and X-ray computed laminography (XCL), are used to measure over-molded modules on a laminate substrate that includes stacked flip-chip Gallium Nitride on Silicon Carbide (GaN-on-SiC) dies. Differences between XCT instruments, XCT instruments versus an XCL instrument, and acquisition parameter settings on 3D reconstructions of the sample are explored. Reference measurement results are compared for image quality, acquisition time, and imaging artifacts. We discuss the current capabilities, limitations, and a potential outlook/roadmap for improving throughput for these types of instruments.

Key words
Semiconductor devices, Non-destructive testing, Imaging artifacts, Failure analysis, Inspection

I. Introduction
Semiconductor devices are becoming more complex as heterogeneous integration is implemented. Three-dimensionally (3D)-stacked chips are one such structure. These structures complicate conventional non-destructive testing (NDT) techniques such as confocal scanning acoustic microscopy (C-SAM) [1]. X-ray-based imaging techniques, on the other hand, can fully penetrate materials, revealing the interior structures. Three-dimensional imaging methods, such as X-ray computed tomography (XCT), can reveal 3D structures and are a popular technique for failure analysis (FA) [2], [3], [4]. There is a growing need for fast inspection methods, which enable defects to be found earlier in the manufacturing process. X-ray computed laminography (XCL) offers benefits for measuring large flat samples, such as wafers or printed circuit boards, by allowing shorter source-to-object distance (SOD) and source-to-detector distance (SDD) at the same magnification as XCT scans, thereby reducing scan time [5], [6]. There is a trade-off with this measurement scheme, often manifesting as imaging artifacts. This paper presents a comparative analysis of X-ray computed tomography (XCT) and X-ray computed laminography (XCL) for 3D-stacked chip inspection, evaluating resolution, scan time, and imaging artifacts under specific tools and their configurations. Given the significant time and resource constraints associated with conducting these evaluations in industrial settings, our baseline findings provide benchmarks to guide XCT/XCL tool selection and optimization, depending on the applications. The key hardware and operational differences between the instruments are detailed.

II. Materials and Methods

A. Sample description
The 3D-stacked chip is composed of a laminate substrate (6 layers) with stacked flip-chip Gallium Nitride on Silicon Carbide (GaN-on-SiC) dies. The mold is about 6 mm × 6 mm × 0.9 mm, as shown in Fig. 1. The laminate substrate is connected to one die via copper (Cu)-pillar bumps, which in

turn are connected to another die stacked on top. An example chip structure is shown from XCT images in section III.B.

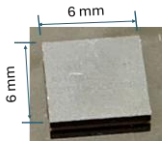


Fig. 1: Image of the chip.

B. XCT and XCL Measurements

Three instruments were used for XCT and XCL measurements. An industrial XCT instrument (denoted as XCT1 in this paper) was used to acquire a macroscopic scan of the module. The instrument is composed of a 225 kV reflection static head source and a flat panel detector (150 µm pixel pitch). Geometric magnification is the primary mechanism for adjusting resolution. Another XCT instrument (denoted as XCT2 in this paper) was used for local (i.e., region of interest) XCT scans (at 1.25 µm/voxel and 0.5 µm/voxel). It is composed of a 160 kV transmission source and a lens-coupled Charge-Coupled Device (CCD) camera (13.5 µm pixel pitch). A 4× objective lens and 2×2 pixel binning were used for the measurements. An XCL instrument (denoted as XCL1 in this paper) was used to acquire XCL scans for this research. It consists of a 160 kV transmission source and a flat-panel detector (49.5 µm pixel pitch). Two voxel resolutions (1.24 µm/voxel and 0.5 µm/voxel) were compared while keeping all other settings nearly identical. We aimed to keep the voxel resolution similar to that used in XCT2 instruments.

Table I shows the scan settings used for the measurements. The XCT2 instrument supports a variable-exposure-time measurement scheme that uses a shorter exposure time when the X-ray is penetrating the flat part of the sample and a longer exposure time when penetrating the thicker part of the sample. For Scan2 and Scan3, the average exposure time is reported in the table and varies within the ranges shown in parentheses. For the scan time, we included only the actual X-ray exposure time for the projections (i.e., exposure time × number of projections), excluding time for stage movements or reference and offset image acquisition. The total acquisition time is an approximate estimate of the scan's start-to-end time. In many instruments, the last images are acquired at the same angle as the first image (0° and 360°). The last image is not included in the reported number of projections.

The voxel edge length (i.e., voxel size/resolution) represents the sampling rate, following geometric and optical magnification. This sampling rate is different from image spatial resolution, which is governed by the instrument's point spread function (i.e., a mathematical convolution of source spot size, scintillator light-blooming effect, and detector pixel size). Although the Nyquist-Shannon theorem [7], [8] suggests that spatial resolution can be approximated as twice the voxel size/resolution, direct measurement via resolution targets or analytical methods such as the modulation transfer function (MTF) is needed for more accurate estimation. However, due to a shortage of standard 3D resolution targets/artifacts across relevant micro- and nano-scale dimensions, evaluations often rely on 2D targets, which may not fully reflect true 3D volumetric resolution. For consistency and practical simplicity, voxel size is used as the nominal spatial metric throughout this paper.

Table I
XCT and XCL acquisition parameters

Measurement	Scan1	Scan2	Scan3	Scan4	Scan5
Instrument	XCT1	XCT2	XCT2	XCL1	XCL1
Voltage (kV)	80	160	160	110	110
Current (µA)	50	62	63	39	23
Filter	Cu[a]	HE1	HE1	None	None
SOD (mm)	16.1	14.0	14.0	16.68	6.68
SDD (mm)	630.8	75.15	187.88	664.43	654.70
Slant angle (°)	0	0	0	22	22
Effective detector pixel (µm)	150	6.71	6.71	49.5	49.5
Voxel edge length (µm)	4.0	1.25	0.5	1.24	0.51
Total scan angle (°)	360	360	360	360	360
Exposure time (s)	1	4.36[b]	28.43[c]	3	3
Number of projections	2250	2000	2200	900	900
Scan time (h)	0.625	2.42	17.37	0.75	0.75
Total acquisition time (h)	1	3.75	17.85	1	1

[a]0.1 mm thickness
[b]Average exposure time; Exposure time varied from 2.3 s to 6.9 s
[c]Average exposure time; Exposure time varied from 15 s to 45 s

C. Tomography vs Laminography

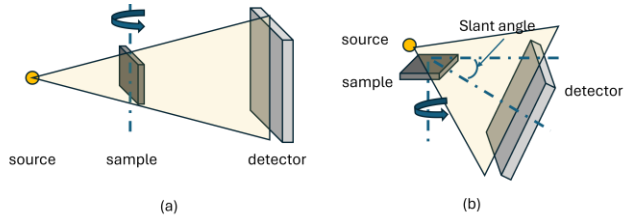


Fig. 2: Comparison of (a) XCT and (b) XCL acquisition modes.

Fig. 2a and b show schematics of XCT and XCL, respectively. A computed tomography scan is generally acquired with the sample rotation axis perpendicular to the X-ray beam axis. Almost complete information is acquired for 3D reconstruction following the Fourier Slice Theorem [9]. There is a small region of missing information due to the cone beam [10], [11]. The chips or printed circuit boards (PCBs) are often measured while mounted vertically, and the effect of imaging artifacts due to the Tuy condition [11] is minimal in typical regions of interest. The Feldkamp-Kress-

Davis (FDK) reconstruction algorithm is often used for the reconstruction due to its high reconstruction speed [12].

A computed laminography scan, on the other hand, has the rotation axis tilted with respect to the beam axis [13], [14]. We consider only rotational laminography, also known as an oblique CT scan. The samples are often mounted horizontally for semiconductor applications, and the beam axis is slightly tilted from the horizontal, forming a slant angle. Because the X-ray beam is tilted, the projection images only fill a portion of Fourier space (i.e., missing cone), leading to blurring in the vertical direction and streaking artifacts at an angle related to the slant angle. The FDK reconstruction algorithm is also used for reconstruction.

III. Analysis and Discussion

A. Different types of instruments

The XCT1 instrument is a typical industrial XCT tool. It is better suited to denser, larger objects such as metal components or PCBs. The small chip used in this research, on the other hand, allows for a smaller SOD compared to the larger objects. The large-area detector (2850 × 2850 pixels with a 150 µm pixel pitch) is well-suited for capturing magnified projection images. The spot size is limited to about 3 µm for a smaller sample that can be placed close to the source. The spot size was estimated to be 4 µm for this measurement.

The main difference between the XCT2 and other instruments is that it uses light-optical magnification in addition to geometric magnification in the imaging chain. As a result, the sample can be placed away from the source, which is beneficial if the sample is large or a test apparatus is used. The main drawback is that this increases the SDD. Since the beam intensity decreases with the square of SDD, the required exposure time increases significantly.
The XCL1 instrument, on the other hand, allows much shorter SOD for flat samples, such as wafers, regardless of their size. Therefore, the SOD and SDD are almost insensitive to the sample size for typical semiconductor devices.

B. Chip structure

The chip is heterogeneously integrated by stacking a laminate and two dies. An example 3D visualization of Scan1 is shown in Fig. 3a, and a vertical cross-sectional image from the Scan1 data is shown in Fig. 3b. The laminate is larger than the two dies, and Die1 is larger than Die2, which sits on top of Die1. The laminate and dies are electrically and mechanically connected via pillar bumps with a diameter of about 75 µm. The pillars are spaced about 150 µm apart.

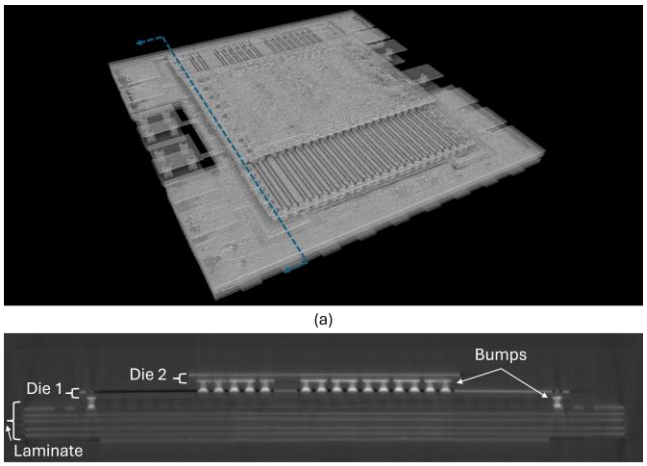


Fig. 3: Visualization of (a) 3D structure and (b) a vertical cross-section.

C. Comparison

The five 3D data sets were manually aligned for comparison. An example measurement result is shown in Fig. 4. The region of interest (ROI) is around the corner where Die1 and the laminate substrate meet. More details are shown in the approximately 1.25 µm/voxel scans (Scan2 and Scan4) and the 0.5 µm/voxel scans (Scan3 and Scan5) than in the 4 µm/voxel scan (Scan1). The hollow through-via in Die1 is clearly shown in the higher-resolution scans (Scan2 and Scan4). Scan1 used a lower X-ray energy (80 kV) than the other scans (110 kV and 160 kV), and it generally shows higher contrast in the pillar bumps. This is because the X-ray attenuation coefficient, which is related to the image contrast, is generally higher at lower X-ray energies. Although the GaN-on-SiC die contrast is low compared to materials in the pillar bump and vias, it is higher than the underfill contrast.

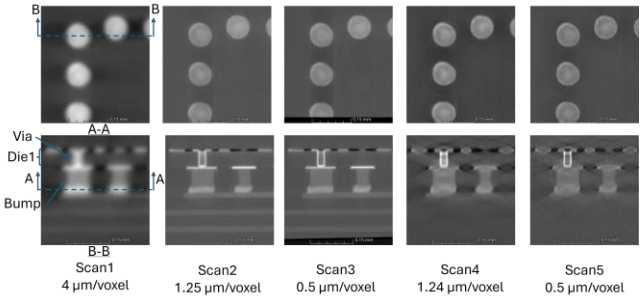


Fig. 4: Comparison of XCT and XCL measurements from three different instruments.

The 0.5 µm/voxel scans (Scan3 and Scan5) reveal more details than the 1.25 µm/voxel scans (Scan2 and Scan4) for both XCT and XCL, as expected. In the XCT scans, darker streaks are visible; these are beam-hardening artifacts caused by pillar bumps aligning along the general X-ray paths. In this case, the streak orientations differ between Scan1 and

Scan2/Scan3 because the samples were mounted differently. These streaks could mask features of interest, such as defects, and decrease their likelihood of detection. The beam-hardening artifacts also appear to reduce the contrast of the high-attenuating regions (e.g., metals) in the X-ray path. Beam-hardening artifacts arise from the polychromatic nature of the laboratory source spectrum, even after filtering. Notably, beam-hardening artifacts are not visible in the horizontal XCL images because the sample was measured at an angle where the X-ray beam doesn't intersect with the arrays of the bumps. The horizontal image quality is visually comparable to XCT scans or better, without beam-hardening artifacts. In vertical cross-sectional images, the XCT reveals clear morphological features of the bumps and shows the laminate's different layers. In contrast, XCL images exhibit artifacts due to the missing cone in Fourier space.

The XCT beam-hardening artifact is more pronounced in the metal layer of Die1, as shown in the left pane of Fig. 5. Beam-hardening artifacts are, again, not visible in the XCL scan (right panel of Fig. 5) because the beam direction never aligns with linear arrays of sample features.

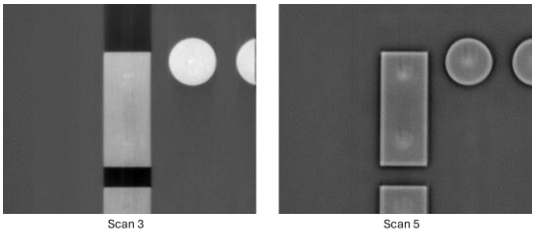


Fig. 5: Comparison of XCT (Scan3) and XCL (Scan5) measurements for beam-hardening artifacts.

The throughput of XCT and XCL is also compared across field-of-view (FOV) sizes and scan time. The flat-panel detector has an advantage over the CCD camera used in this research because of its larger array. It is recommended to bin the CCD camera pixels by two to improve the signal-to-noise ratio (SNR), reducing the achievable FOV by two. In this case, the XCL1 instrument can measure an area about 6.5× larger than the XCT2 instrument. The FOV sizes are compared in more detail in Table II. The usable region in a 3D volume is a cylindrical area. The FOV sizes are visually compared in Fig. 6. The Scan4 data covered almost ¼ of the sample at a 1.25 µm/voxel resolution.

Table II
FOV Size Comparisons

Measurement	Detector pixel count	Detector FOV (mm^2)	3D volume (mm^3)
Scan1	2850 × 2850	11.4 × 11.4	11.4 × 11.4 × 11.4
Scan2	1024 × 1024	1.28 × 1.28	1.28 × 1.28 × 1.28
Scan3	1024 × 1024	0.51 × 0.51	0.51 × 0.51 × 0.51
Scan4	2940 × 2304	3.65 × 2.86	3.65 × 3.65 × 2.86
Scan5	2940 × 2304	1.50 × 1.18	1.50 × 1.50 × 1.18

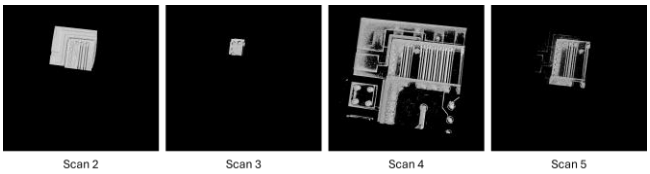


Fig. 6: Visual comparison of FOV size from the 3D volume.

The XCL1 instrument did not use any filter, which is typically required for XCT measurements to harden the beam spectrum and reduce beam-hardening imaging artifacts. Beam-hardening artifacts remained visible in XCT scans despite the use of a filter. The filtering process reduces the X-ray flux, which affects the exposure time. Due to the relatively short, constant X-ray penetration path in laminography mode, beam-hardening artifacts are not visible in the horizontal cross sections, resulting in shorter exposure times.

The exposure time increased significantly for the 0.5 µm/voxel XCT scan (Scan3) over the 1.25 µm/voxel XCT scan (Scan2). Table III shows exposure time and some image quality parameters measured over 128 × 128-pixel regions in the center of the images. For Scan2 and Scan3, the reference image exposure times were 2.3 s and 15 s, respectively. Since the SDD was increased by about 2.5 times, an equivalent increase in exposure time of about 6.25 times is expected to yield the same signal level. In this case, the exposure time was increased by about 6.5 times, resulting in a similar SNR in the reference radiography images. The XCL scans, on the other hand, achieved similar SDD for two scans (0.51 µm/voxel and 1.24 µm/voxel), and the same exposure time was used.

Table III
Comparison of Reference Image Quality of Scan2 and Scan3

Measurement	Ref exp. time (s)	Signal (Gray level)	Noise (Gray level)	SNR
Scan2	2.3	8492.1	82.6	102.8
Scan3	15	8282.5	78.7	105.2

Two 3D ROIs were used to measure SNR and contrast-to-noise ratio (CNR) in the reconstructed images: one in the middle of the pillar (ROI1) and one outside of the pillar (ROI2), as shown in Fig. 7. The SNRs reported in Table III are measured from 2D reference radiographs, and the values in Table IV are extracted from 3D reconstructed images. Relatively shallow ROIs were used to mitigate potential effects of non-uniformity in the sample materials and vertical blurring in the XCL data. Additional research is required to establish the ROI selection criteria for XCL measurements. ROI2 (outside of the pillar) is expected to have underfill material, but the contrast is very low due to low X-ray

attenuation. The contrast was computed as the signal difference between ROI1 and ROI2, and the noise (standard deviation) from ROI2 was used to compute the CNR. The results are shown in Table IV. Both SNR and CNR generally decrease with higher-resolution scans. Similar SNR and CNR measurements were achieved for XCT and XCL scans in this case (Scan3 versus Scan5).

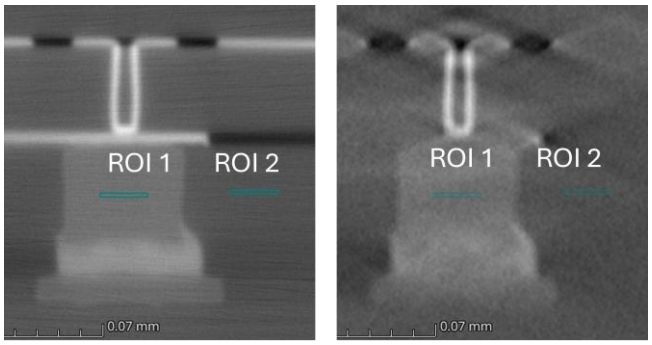


Fig. 7: ROIs used to measure signals and noise.

Table IV
Image Intensity, Noise, SNR, CNR of Two ROIs

	Scan2	Scan3	Scan4	Scan5
ROI1 Intensity (Gray level)	30472.1	28470.5	31728	30197.2
ROI1 noise (Gray level)	331.9	845.5	498.9	809.4
ROI2 Intensity (Gray level)	24409.4	22385.9	23170.4	24437.4
ROI2 noise (Gray level)	281.3	748	382.4	808.7
ROI1 SNR	91.8	33.7	63.6	37.3
ROI2 SNR	86.8	30.0	60.6	30.2
CNR	21.5	8.1	22.4	7.1

IV. Conclusion

This paper presents a systematic comparison of XCT and XCL imaging methods for 3D-stacked chip configurations, providing reference measurements of key variables, such as voxel resolution, scan time, and imaging artifacts (e.g., beam-hardening and laminography artifacts) to guide the integration of NDT tools for advanced packaging inspection. Our measurements demonstrate that XCL can overcome the severe throughput limit of sub-micrometer XCT scans while reducing beam-hardening artifacts observed in typical XCT scans of semiconductor devices. Although laminography imaging artifacts are present in vertical image cross-sections, the significant gain in throughput positions XCL as a viable alternative for rapid FA and process improvements.

These results reflect the measurement performance under specific sample geometries, tool configurations, and scan parameters. While the current results show great promise for XCL, they were not obtained at the in-line/near-line inspection level. Further investigation is needed to demonstrate the feasibility. The sub-micrometer XCL scans still captured a portion of the sample, and a careful sampling strategy may be needed for inspection processes, especially for wafer-level samples. A reconstruction-less detection process using fewer projections may be feasible for samples with simpler structures to expedite inspection time, but more research is needed. The XCT2 instrument used in this research is an older model; newer systems may offer higher throughput with enhanced hardware and software capabilities in tomography mode. Future research will investigate the effects and trade-offs of various acquisition/reconstruction parameters for XCT and XCL measurements, suggesting directions for improving throughput and image quality.

Acknowledgment

We would like to acknowledge Qorvo[i] for providing samples.

References

[1] N. Varshney, S. Ghosh, P. Craig, H. R. Kottur, H. Dalir, and N. Asadizanjani, “Challenges and opportunities in non-destructive characterization of stacked IC packaging: insights from SAM and 3D x-ray analysis,” in *Developments in X-Ray Tomography XV*, SPIE, Oct. 2024, p. 415. doi: 10.1117/12.3027317.

[2] C. Hartfield, C. Schmidt, A. Gu, and S. T. Kelly, “From PCB to BEOL: 3D X-Ray Microscopy for Advanced Semiconductor Packaging,” in *2018 IEEE International Symposium on the Physical and Failure Analysis of Integrated Circuits (IPFA)*, Jul. 2018, pp. 1–7. doi: 10.1109/IPFA.2018.8452551.

[3] M. Pacheco and D. Goyal, “Detection and characterization of defects in microelectronic packages and boards by means of high-resolution x-ray computed tomography (CT),” in *2011 IEEE 61st Electronic Components and Technology Conference (ECTC)*, May 2011, pp. 1263–1268. doi: 10.1109/ECTC.2011.5898673.

[4] E. Zschech, W. Yun, and G. Schneider, “High-resolution X-ray imaging—a powerful nondestructive technique for applications in semiconductor industry,” *Appl. Phys. A*, vol. 92, no. 3, pp. 423–429, Aug. 2008, doi: 10.1007/s00339-008-4551-x.

[i] Disclaimer: Any mention of commercial products within this manuscript is for information only; it does not imply recommendation or endorsement by NIST.

[5] T. Dreier, D. Nilsson, and J. Hållstedt, “Fast and high-resolution X-ray nano tomography for failure analysis in advanced packaging,” *Microelectronics Reliability*, vol. 168, p. 115694, May 2025, doi: 10.1016/j.microrel.2025.115694.
[6] S. H. Lau *et al.*, “Next-Gen Failure Analysis: 3D X-Ray Imaging at 350 nm Meets Laminography,” in *2025 IEEE 32nd International Symposium on the Physical and Failure Analysis of Integrated Circuits (IPFA)*, Aug. 2025, pp. 1–6. doi: 10.1109/IPFA65338.2025.11256626.
[7] C. E. Shannon, “Communication in the Presence of Noise,” *Proceedings of the IRE*, vol. 37, no. 1, pp. 10–21, Jan. 1949, doi: 10.1109/JRPROC.1949.232969.
[8] H. Nyquist, “Certain Topics in Telegraph Transmission Theory,” *Transactions of the American Institute of Electrical Engineers*, vol. 47, no. 2, pp. 617–644, Apr. 1928, doi: 10.1109/T-AIEE.1928.5055024.
[9] A. C. Kak and M. Slaney, *Principles of Computerized Tomographic Imaging*. in Classics in Applied Mathematics. Philadelphia, PA: Society for Industrial and Applied Mathematics, 2001.
[10] B. D. Smith, “Image reconstruction from cone-beam projections: necessary and sufficient conditions and reconstruction methods,” *IEEE Trans Med Imaging*, vol. 4, no. 1, pp. 14–25, 1985, doi: 10.1109/TMI.1985.4307689.
[11] H. K. Tuy, “An Inversion Formula for Cone-Beam Reconstruction,” *SIAM Journal on Applied Mathematics*, vol. 43, no. 3, 1983, doi: 10.1137/0143035.
[12] L. A. Feldkamp, L. C. Davis, and J. W. Kress, “Practical cone-beam algorithm,” *J. Opt. Soc. Am. A, JOSAA*, vol. 1, no. 6, pp. 612–619, Jun. 1984, doi: 10.1364/JOSAA.1.000612.
[13] W. Du *et al.*, “X-ray computed laminography: a brief review of mechanisms, reconstruction, applications and perspectives,” *Materials Today*, vol. 86, 2025, Accessed: Jun. 06, 2026. [Online]. Available: https://ora.ox.ac.uk/objects/uuid:d07c136b-fb48-4ecf-965c-d128463fbea3
[14] R. Lu, P. He, G. Chen, and M. Fang, “A Review of Computed Laminography Technology: Principle, Artifact Suppression, and Applications,” *IEEE Transactions on Instrumentation and Measurement*, vol. 75, pp. 1–24, 2026, doi: 10.1109/TIM.2026.3659586.